International Journal of Heat and Mass Transfer 115 (2017) 377–386

Contents lists available at ScienceDirect

International Journal of Heat and Mass Transfer

journal homepage: www.elsevier.com/locate/ijhmt

# Mass transfer performance of water recovery from flue gas of lignite boiler by composite membrane

Fuxiang Zhang [a], Zhihua Ge [a], Yinli Shen [a], Xiaoze Du [b,a,*], Lijun Yang [a]

[a] Key Laboratory of Condition Monitoring and Control for Power Plant Equipment (North China Electric Power University), Ministry of Education, Beijing 102206, China
[b] School of Energy and Power Engineering, Lanzhou University of Technology, Lanzhou 730050, China

ARTICLE INFO

*Article history:*
Received 30 January 2017
Received in revised form 22 June 2017
Accepted 10 July 2017
Available online 21 July 2017

*Keywords:*
Moisture flue gas
Membrane separation
Stefan Maxwell theory
Mass transfer
Multiple attribute decision making

ABSTRACT

Membrane technology is a potential way for water recovery from the flue gas of the lignite boiler. Consider the influences of the micro-scale configuration of the membrane and the operating parameters, the physical process was modeled based on the Stefan Maxwell theory, as well as the composite membrane resistance model for numerical simulation. The mass transfer process of flue gas in coating, transition layer and support layer of the composite membrane was analyzed respectively. The theoretical results were both verified by experiments and numerical simulations. The influences of different materials, pressure difference, porosity and transition layer thickness on the water vapor permeation flux were revealed. The results show that the high Henry coefficient and the high selectivity of water vapor have great advantages in the application, and the increase of pressure, porosity and thickness of the transition layer are all beneficial to increase the water vapor flux. Based on the theoretical model, the multi attribute decision making method was employed to provide suggestions for membrane material selection of gas water recycling in the experimental researches as well as in the engineering applications.



## 1. Introduction

The utilization of lignite in coal-fired power plants of China will continue to increase in the future, leading to that the water percentage of the flue gas can be as high as 16%. Membrane technology has been proved to be a high qualified approach for component separation [1–3]. In addition, there are numerous researches about the water recovery from wet flue gas by membrane technology, including that of the model calculation, CFD simulation and experimental verification [4–9]. However, the transport mechanism and the refined description of mass transfer process in the membrane were less involved.

According to the pore level model of the separation membrane and the relationship between the gas and the membrane, the multi component gas separation principle consists of micro pore diffusion, dissolution diffusion and composite membrane resistance model [10–12]. The previous studies mainly used the Fick's law [13] to explain the component transfer process. However, the Fick diffusion was driven by the concentration gradient, but in practical applications, the separation of gas mainly depends on the pressure gradient. More comprehensive study [14] showed that at least in the early stage of the multi-component mixture diffusion, the diffusion coefficient was not related to its concentration, implying that mere concentration diffusion did not suit for the separating process of multicomponent flue gas.

As a comparison, the Maxwell Stefan theory considers the effects of non-ideal thermodynamics and external force fields, which can better describe the multi-component diffusion in complex configuration than that of the Fick's law. The Maxwell Stefan theory has universal applications in analysis of the separation process of the mixture. For example, Grahn et al. [15] and Kangas et al. [16] used Maxwell Stefan theory to study the physical processes of mixed $CO_2/H_2$ separation. Costa-Corredo et al. used this theory to simulate the water and salt diffusion process [17]. Several investigations [18–20] used Maxwell Stefan theory, Fick's law and the so-called dust and gas model to analysis the physical phenomena of protein absorption anion. It was found that the Maxwell Stefan theory had its own irreplaceable advantages.

Based on the literature review, the physical process of water recovery of coal-fired boiler exhaust flue gas by membrane technology is modeled based on the Stefan Maxwell theory, as well as the composite membrane resistance. The influences of micro-scale configuration of the membrane and the operating parameters on the performance of water transport are discussed herewith. According to the results, the suggestions are given to the material

* Corresponding author.
*E-mail address:* duxz@ncepu.edu.cn (X. Du).

http://dx.doi.org/10.1016/j.ijheatmasstransfer.2017.07.037
0017-9310/

**Nomenclature**

| | |
|---|---|
| $A$ | Avogadro's number, $mol^{-1}$ |
| $B$ | hydraulic permeability coefficient |
| $C^*$ | comprehensive evaluation index |
| $c$ | average concentration of the mixture through the layer, mol $m^{-3}$ |
| $D$ | Maxwell Stefan diffusion coefficient, $m^2\ s^{-1}$ |
| $d$ | diameter, m |
| $F$ | driving force, N $mol^{-1}$ |
| $f$ | embedding rate |
| g | the value after vector specification |
| $h$ | weighted norm |
| $M$ | mole mass, kg $mol^{-1}$ |
| $N$ | gas permeation, mol $m^{-2}\ s^{-1}$ |
| $p$ | gas partial pressure, N $m^{-2}$ |
| $R$ | gas constant, J $mol^{-1}\ K^{-1}$ |
| $s$ | number of data |
| $T$ | temperature, K |
| $t$ | comprehensive weight |
| $W$ | entropy value |
| $w$ | weight |
| $x$ | mole fraction of $j$ |
| $y$ | table attribute value |
| $z$ | layer thickness, m |

*Greek symbols*

| | |
|---|---|
| $\gamma$ | contraction factor |
| $\varepsilon$ | porosity |
| $\lambda$ | expert weight |
| $\xi$ | friction coefficient, N s $mol^{-1}\ m^{-1}$ |
| $\Psi$ | component potential, J $mol^{-1}$ |
| $\tau$ | path factor |

*Subscripts*

| | |
|---|---|
| $d$ | the "dust" which represents the membrane in "dust-gas" model |
| dis | dissolved permeability |
| $i$ | component $i$ |
| $j$ | component $j$ |
| $m$ | row |
| $n$ | column |
| K | Knudsen diffusion |
| $p$ | pore of membrane |
| $v$ | viscous flow |

selection of the composite membrane in the experimental researches as well as in the engineering applications.

## 2. Process description

The typical components of the exhaust flue gas of coal-fired boiler of a 300 MW power generating unit with lignite as fuel are $H_2O$, $N_2$, $CO_2$, $O_2$ and a small amount of $SO_2$ and $NO_2$. Their mass fractions are 5–11%, 72–75%, 13–16%, 0.35–1%, respectively. In this study, the mass fraction, mole fraction, density and viscosity of each component at the outlet temperature of the outlet flue gas, 110 °C, are shown in Table 1.

It has been widely proposed that the multi-layer membrane is used to separate the components of exhaust flue gas in the coal-fired power plant [21,22]. According to the structure, the membrane can be divided into symmetrical and asymmetrical ones, including four main groups based on the nature of the membrane material: polymeric, inorganic, mixed-matrix and liquid membranes [1–3]. At present, hollow fiber membrane, ceramic membrane, zeolite membranes and glass fiber membrane are commonly used.

In practice, the membrane separation device is located after the desulfurization and denitration equipment in the chimney of the coal fired power plant boiler. The flue gas that flows through the membrane module is divided into the pipe flow and the outer flow according to the flue gas goes inside or outside of the membrane tube bundles. Also the flow modes can be described as concurrent, countercurrent and cross flow based on the relative position of the direction of flue gas flow and the pipes.

Fig. 1(a) and (b) shows the schematic diagram and the practical cross flow membrane separation module, respectively. The direction of flue gas flow and that of the membrane pipe bundles are vertical arrangement. The saturated flue gas stream flowed at the outside of the membranes. A vacuum was applied inside membranes to provide a driving force for water vapor permeation. The water vapor component in the flue gas can be trapped and collected in a condense cooler. Composite hollow fiber membranes with a top layer of SPEEK were built into fiber bundles.

## 3. Physico-mathematical models

In this paper, the hollow fiber membrane is employed as the physical model, which separates the flue gas based on its selectivity to different components and the potential difference on the both sides of the membrane. It has been verified that the membrane material selected in this study has much higher water vapor permeability than that of other inert components in the flue gas [8].

### 3.1. Physical model

Dense layer of hollow fiber membrane locates outer surface or inner surface of the fiber, and it constitutes the external and internal pressure difference, which becomes the driving force of mass transfer. The membrane material has good selectivity to different components, only water vapor can pass through the membrane pores, while the other gas molecules can hardly pass.

**Table 1**
Components and physical properties of the exhaust flue gas.

| | $H_2O$ | $N_2$ | $O_2$ | $CO_2$ | $SO_2$ and $NO_2$ |
|---|---|---|---|---|---|
| Mass fraction (%) | 11 | 72 | 4 | 13 | 1 |
| Mole fraction (%) | 17.08 | 71.88 | 3.5 | 6.99 | 0.55 |
| Density, $\rho$ ($kg/m^3$) | 0.83 | 0.891 | 0.98 | 1.34 | 0.87 |
| Viscosity, $\eta \times 10^6$ (Pa s) | 12.425 | 22 | 25 | 1960 | 14 |

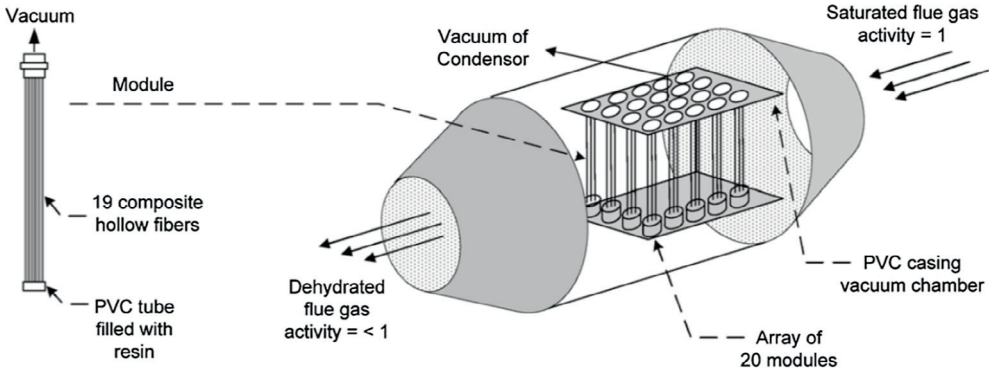


(a) Schematic diagram of polymer membranes modules.

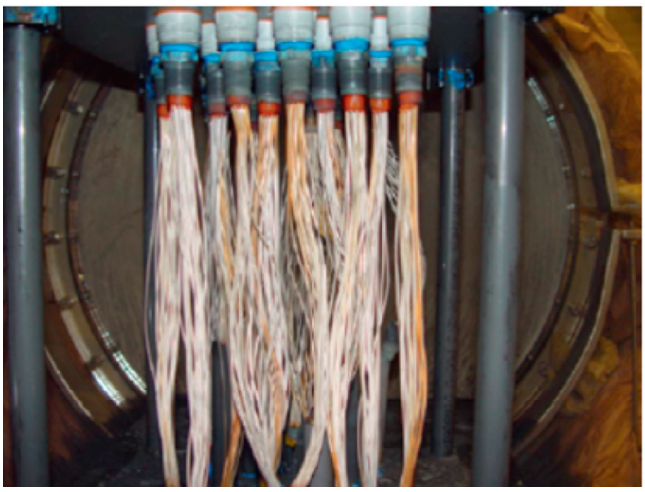

(b) The practical cross-flow membrane separation module.

**Fig. 1.** Physical model to illustrate the flue gas dehydration by polymer membranes [8].

The microstructure of the composite membrane employed for water recovery of the flue gas is shown in Fig. 2(a), as well as the three-layer configuration is simplified illustrated in Fig. 2(b). The coating, connecting and support layers of the composite membrane, are respectively indicated as $L_1$, $L_2$ and $L_3$ in Fig. 2(b). The coating layer is of compact structure, which can be regarded as a porous membrane without the consideration of the pore level impact. The component diffusion in the coating can be considered as dissolution penetration. The support layer is of larger gap than that of coating layer, of which the most pore sizes are in the range of 10–20 μm, as shown in Fig. 1(a). For the cases and transport parameters present studied, the viscous flow and Knudsen diffusion exist simultaneously. The connecting layer between the coating and supporting layers with the average pore size of about 0–10 μm, both dissolution penetration and Knudsen diffusion should be taken into consideration.

### 3.2. Maxwell Stefan theory

Forces acting on the mixture passing through the membrane can be divided as driving forces and friction forces. The basic idea of Maxwell Stefan theory is that the friction forces should be equal to the driving forces. The Stefan Maxwell equation is the result of these two types of forces,

$$F_i = \xi_{i,j} x_j (u_i - u_j) \tag{1}$$

in which, $F_i$ is the driving force, $\xi_{i,j}$ is the friction coefficient between components $i$ and $j$, $x_j$ is the mole fraction of component $j$, $u_i$, $u_j$ in m/s are the diffusion rate of components $i$ and $j$, respectively.

In a more common format, the friction coefficient can be revised to the Stefan Maxwell diffusion coefficient as follows,

$$D_{i,j} = \frac{RT}{\xi_{i,j}} \tag{2}$$

where $D_{i,j}$ in $m^2/s$ is the Stefan Maxwell diffusion coefficient between components $i$ and $j$, $R$ is the ideal gas constant, $T$ in K is the local temperature.

The force per unit volume of component $i$ in N/(mol $m^3$), $f_i$, also can be obtained by the flow flux of each component of the flue gas,

$$f_i = \sum_{j \neq i} \frac{RT}{D_{i,j}} (x_j N_i - x_i N_j) \tag{3}$$

in which, $N_i$ and $N_j$ in mol/($m^2$ s) are the gas permeation of components $i$ and $j$, respectively, $xi$ is the mole fraction of $i$.

$f_i$ can not be obtained directly from the experiment or simulation, so we use a different form to express the diffusion coefficient, $D_{i,j}$, by the ratio of the potential difference and the film thickness,

$$-\overline{x}_i \frac{\Delta \Psi_i}{\Delta z} = \sum_{j \neq i} \frac{RT}{\overline{c} D_{i,j}} (\overline{x}_j N_i - \overline{x}_i N_j) \tag{4}$$

where $\Psi_i$ in J/mol is the potential energy of component $i$, $c$ in mol/$m^{-3}$ is the average flue gas flow concentration of both sides of the membrane, and $z$ is lawyer thickness.

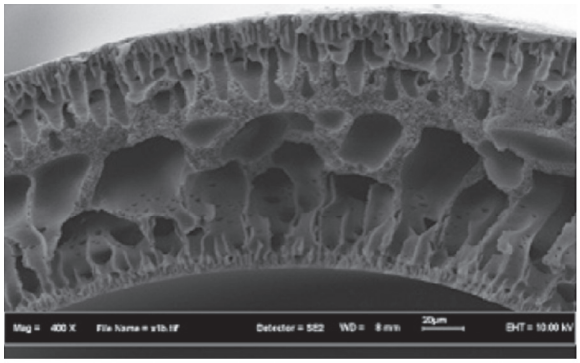

(a) SEM images of hollow fiber membrane [23].

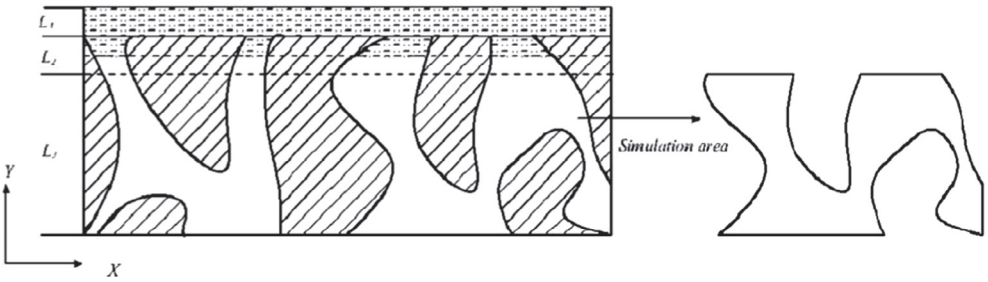


(b) Three layer structure.

**Fig. 2.** Configuration of the composite membrane used to separate the components in flue gas.

The Stefan Maxwell diffusion coefficient, $D_{i,j}$, of flue gas components inside the composite membrane can be obtained by the theory of gas dynamics and dust-gas model. Assuming that the gas molecules are hard sphere, and the friction between the components is due to the momentum exchange between different molecules in the collision, the expression of diffusion coefficient then can be acquired by,

$$D_{i,j} = \sqrt{\frac{2}{\pi^3}} \frac{(RT)^{3/2}}{Apd_{i,j}^2} \left(\frac{1}{M_i} + \frac{1}{M_j}\right)^{1/2} \tag{5}$$

in which, $d_{i,j} = \frac{d_i + d_j}{2}$, $d_i$, $d_j$ are the molecule diameters of components $i$ and $j$, respectively, $M_i$ and $M_j$ in kg/mol are the molar mass of the two substances, respectively, $A$ is the Avogadro's number, $p$ is the gas partial pressure.

Because the particles that composed the membrane matrix is much bigger than that of the gas components, the dust-gas model [13,24] and formula are employed to describe the diffusion coefficient between the flue gas components and the membrane. The membrane matrix particles are regarded as the giant ideal gas molecules, of which the mole mass and diameter of the "dust" are indicated as $M_d$ and $d_d$, respectively. It is assumed that $M_d \gg M_i$ and $d_d \gg d_i$. Hence the diffusion coefficient of "dust", $D_{i,d}$,can be written as,

$$D_{i,d} = \frac{2^{5/2}}{\pi^{3/2}} \frac{(RT)^{3/2}}{Apd_d^2} \frac{1}{M_i^{1/2}} \tag{6}$$

Considering the membrane matrix as well as the fluid around the matrix as a whole, the "dust" does not represent the complete membrane matrix. The diffusion coefficient between membrane and flue gas component is related to the mole fraction of the surrounding gas. It is necessary to use the mole fraction of "dust" to solve the diffusion coefficient between gas and membrane matrix,

$$x_d = \frac{n_d}{n_i + n_j + n_d}, n_d = \frac{1-\varepsilon}{\frac{\pi}{6} d_d^3}, n_i + n_j + n_d = \frac{pA}{RT}, \tag{7}$$

in which, $x_d$ is mole fraction of "dust", and the amount of substance "dust", component $i$ and component $j$ are indicated as $nd$, $n_i$, $n_j$, respectively, $\varepsilon$ is the porosity of the membrane discussed.

By combining Eqs. (6) and (7), the diffusion coefficient between membrane and flue gas components can be obtained by,

$$D_{i,m} = \frac{D_{i,d}}{x_d} = \frac{d_d}{1-\varepsilon} \sqrt{\frac{8}{9\pi} \frac{RT}{M_i}} \tag{8}$$

However, despite of its widely applications, it was found that some transport phenomena might be free from the problematic aspect of dusty gas model. Kerkhof found that the invalid of the dusty gas approach was mainly in the region where viscous friction dominated [25]. For the present transport phenomena, Knudsen diffusion and dissolution penetration dominate respectively in all three layers. Only in the support layer viscous flow and Knudsen diffusion exist simultaneously. The dust-gas model is employed herewith to obtain the diffusion coefficient as mentioned above.

In the process of mass transfer, the diffusion coefficient between gas and membrane has its particularity. The space part of the membrane is actually the hole with different width and contraction, which influences the diffusion coefficient significantly and hence cannot be ignored. This effect is called the tortuous effect, which increases route and gas diffusion rate at the constant flux. By considering the tortuous effect, the diffusion coefficient of Stefan Maxwell between the different gases or between gas and matrix can be amended by [14],

$$\mathrm{D}_{i,j}^* = \mathrm{D}_{i,j} \frac{\gamma}{\tau^2} \quad D_{i,m}^* = \mathrm{D}_{i,\mathrm{m}} \frac{\gamma}{\tau^2} \tag{9}$$

where $\gamma$ is contraction factor, $\tau$ is the path factor, $D_{i,j}{}^*$ and $D_{i,m}{}^*$ have taken into account the twists and turns effect. The following discussions will use $D_{i,j}$, $D_{i,m}$ instead of $D_{i,j}{}^*$, $D_{i,m}{}^*$.

### 3.3. Mass transfer of flue gas components through the composite membrane

#### 3.3.1. The coating layer

Because there are corresponding purification facilities before the flue gas exhausting, there are little components of $SO_2$ and $NO_2$. Therefore, the present study only discusses the first four kinds of components of the flue gas listed in Table 1.

The selectivity and permeability of the coating layer are mainly depended on to realize components separation. The differential form flux of Maxwell Stefan equation to represent the component diffusion equation can be then obtained by,

$$-\overline{x}_i \frac{\Delta p_i}{\overline{p}_i \Delta z} = \sum_{j=1}^{n} \frac{\overline{x}_j N_i - \overline{x}_i N_j}{D_{i,j}\overline{c}} + \frac{N_i}{D_{i,M}\overline{c}} \tag{10}$$

$i, j$ = 1, 2, 3, 4 represents $H_2O$, $N_2$, $O_2$ and $CO_2$, respectively. The pore size of coating is small, hence the friction force between the components of the flue gas can be ignored comparing the friction force between gas and membrane,

$$N_i = -\frac{D_{i,m}}{\Delta z} He_i \Delta p_i \tag{11}$$

of which, $He_i$ in mol/(m$^3$ Pa) is the Henry constant of component $i$.

It can be obtained from Eq. (11) that the permeability of the gas in the coating layer of the composite membrane is related to gas pressure and gas solubility of the coating.

#### 3.3.2. The connecting layer

As shown in Fig. 2(b), the connecting layer includes both defective porous part and compact structure similar to the coating layer, which belongs to the dissolved penetration, while the defective porous part exists micro diffusion. Because the gap is in microscale in this area, the Knudsen diffusion dominates. Assuming that the pores are uniform distribution, the Knudsen diffusion and dissolved permeability respectively can be expressed by,

$$-\overline{x}_i \frac{\Delta p_i}{\overline{p}_i \Delta z} \varepsilon = \sum_{j=1}^{n} \frac{\overline{x}_j N_{i,K} - \overline{x}_i N_{j,K}}{D_{i,j}\overline{c}} + \frac{N_{i,K}}{D_{i,M}\overline{c}} \quad (j = 1,2,3,4) \tag{12}$$

$$N_{i,dis} = -\frac{D_{i,m}}{\Delta z} He_i \Delta p_i (1-\varepsilon) \tag{13}$$

where $N_{i,k}$ and $N_i$,$d_{is}$ are the gas permeation of the $i$th component in Knudsen diffusion and in dissolved permeability, respectively. The composite membrane resistance theory shows that the total flux is the sum of the two fluxes. Hence,

$$N_{i,sum} = N_{i,K} + N_{i,dis} \tag{14}$$

To sum up, the pressure difference and the thickness of the conencting part are the main factors affecting the flux in connecting layer.

#### 3.3.3. The support layer

Although the viscous flow in narrow pores is small, the flow velocity increases with pore size. The character size of the channel in supporting layer is larger than that of the first two layers, so that the viscous flow cannot be ignored. The supporting layer can be taken as porous media either, while diffusion velocity and viscous flow velocity exist simultaneously.

The expression of Knudsen diffusion represented by Stefan Maxwell equation also can refer to Eq. (10). The mass transfer equation of viscous flow is shown as,

$$F_i = \xi_v v \tag{15}$$

in which, $\xi_v$ in N/(s mol m) is the viscous friction coefficient, and $v$ is viscous flow velocity.

The left side of Eq. (15) is the driving force, and the right is the friction. The viscous friction coefficient is related to the hydraulic permeability of the structure. While transferring in a cylindrical hole, it can be obtained by,

$$\xi_v = \frac{\eta}{cB} \quad B = \frac{d_p^2}{(1-\varepsilon)^2} \tag{16}$$

in which, $\eta$ in Pa·s is the viscosity, B is the hydraulic permeability coefficient, $d_p$ is the pore diameter.

The expression for the viscous flow velocity is,

$$v = \frac{1}{32} \frac{-\Delta p d_p^2}{\eta \Delta z} \tag{17}$$

The total flux of the components is the sum of the fluxes of those two flow modes. The model indicates that the flux of each component in the flue gas through the composite membrane is related to the pressure difference, viscosity, pore size and so on.

## 4. Theoretical model validation

### 4.1. Experimental verification

In this section, the experimental results from references [10] were quoted to verify the above theoretical model. The material is hollow fiber membrane prepared by PVDF basement membrane, and RTV-10$^7$ coating. The gas is a mixture of 4% n-heptane and 96% nitrogen, and the operating temperature is 303.5 K while the mixed gas flow rate is 500 mL/min. In this experiment, the penetration rate of n-heptane ($C_7H_{16}$) is $1.5 \times 10^{-7}$ mol/(m$^2$ s Pa), and the separation ratio of $C_7H_{16}$ and $N_2$ was 470. The permeate pressure is 6.9 kPa, and feed pressure changes from 200 kPa to 600 kPa. The configuration, as well as the preparation by dip-coating method of $C_7H_{16}$ is similar to the following studied composite membranes. Hence, they have the transport mechanism, and have the common theoretical model of Maxwell Stefan theory.

Maxwell Stefan theoretical model was used to calculate the permeability of $C_7H_{16}$ under different pressure conditions. The results were compared with the experimental values, which was shown in Fig. 3.

With the increase of feed pressure, it can be found that the $C_7H_{16}$ permeability increases by either the theoretical results or the experimental values. The theoretical predictions and the experimental results are in a well agreement by considering their aver-

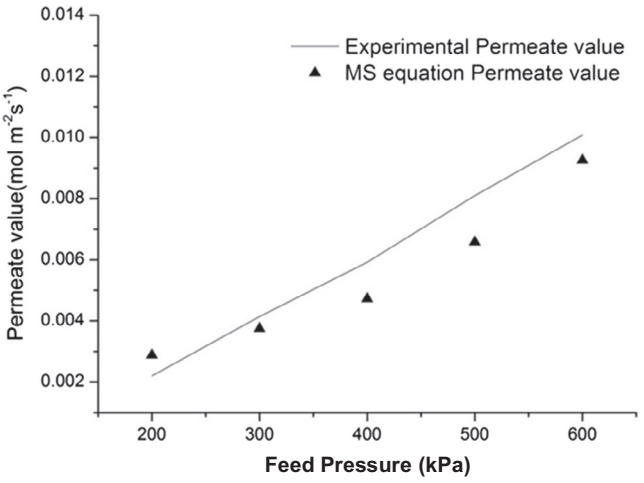


**Fig. 3.** Comparison of $C_7H_{16}$ permeability between experimental results [10] and theoretical predictions at different feed pressures.

age absolute percentage deviation is no more than 10%. This may indicate that the model can meet the requirements of calculation of water vapor flux in multi component gas separation. However, because of the absence of the experimental data uncertainty analysis in the Ref. [10], only the tendency agreement can be verified by Fig. 3.

### 4.2. Simulation verification

In this paper, the coating layer of the composite membrane is dissolved penetration while the connecting lawyer is a combination of dissolved penetration and micro diffusion. The simulation verifies mainly at support layer. As mentioned above, two-dimensional physical model is established based on the configuration of the support layer with the character size of $10^{-4}$ m. It is believed that the continuous medium theory and the Navier-Stokes equations are still applicable to the medium with a character diameter of 1 $\mu m^{-1}$ mm [26].

The simulation domain of the present physical composite membrane is 200 μm in thickness, and the porosity is 0.54. Assume that the flue gas, with the components of $H_2O$, $N_2$, $CO_2$ and $O_2$, respectively, is a continuous medium with laminar flow, uniform inlet velocity and uniform heat flux density. Set the inlet and outlet pressures as the boundary conditions. The surface heat transfer coefficient is set to be 0.2 W/($m^2$ K) while the temperature outside the flue and the exhaust gas temperature before entering the chimney are 300 K and 383 K, respectively. The interface between solid and fluid is no-slip. The other conditions use the default parameters.

This study uses Gambit to establish a mesh model for the present physical model, which discretizes the calculating domain and the boundaries shown in Fig. 2(b). The residuals of the simulation are set to be less than $10^{-6}$.

Fig. 4 shows the velocity contours through the support layer of the membrane at the pressure difference of 6 kPa and 10 kPa, respectively. After the separation of the coating and the connecting layer, the dialysis material in the support layer is water vapor and a small amount of gas and other gas. The velocity of fluid flow is related to the shape and size of the flow area and the speed of the narrow part increases quickly. It implies that the tortuous effect has a great influence on flow effect. When the pressure difference increases, the fluid flow rate increases at the same time. At this point, the support layer doesn't have selection ability, where the pressure drop dominates the mass transfer.

The simulation results are compared with the theoretical calculation results under the same conditions. When the pressure difference changes in the range of 6kPa to 20kPa, the results are illustrated in Fig. 5.

The results indicate that the theoretical and simulating values are of larger difference when the pressure difference is small. This can deduce to the Knudsen effect may dominates the diffusion under low pressure difference, which does not considered in the present simulation. However, with the increment of the pressure difference, the deviations between the prediction of theoretical model and that of numerical simulation are gradually reduced. And the tendency respectively obtained by the theoretical model and numerical simulation is coincident.

Combining the verifications both from the experimental data and the numerical simulation, it can be concluded that the Maxwell Stefan theoretical model can have a high precision under the determined operating conditions. Hence, the following discussions mainly base on the theoretical results obtained by the present established model.

## 5. Results with discussions

The initial concentration of mixture in each layer of the composite membrane can be set to be the outlet concentration of previous layer. The coating material properties, porosity of the membrane, the connection layer thickness, temperature are all affecting the water vapor flux in the membrane.

In the previous studies [3,23,27,28], lots of materials, including that of cellulose acetate, polyimide and so on, were employed as the separating membrane both by experiments and simulations. Table 2 lists the water vapor permeability and gas selective performance of some commonly used materials, in which, the unit of permeability, Barrer, can be expressed in SI unit as 1Barrer = $0.76 \times 10^{-17}$ $m^3$ (STP)·m $m^{-2}$ $s^{-1}$ $Pa^{-1}$.

Materials must be satisfied with high water vapor permeability and high gas selectivity. In this paper, the mole fraction of water vapor, nitrogen, oxygen and carbon dioxide in the exhaust flue

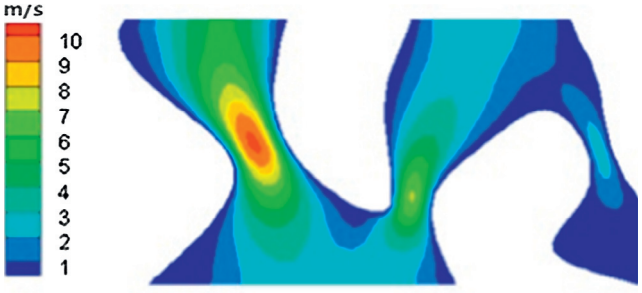


(a) 6kPa.

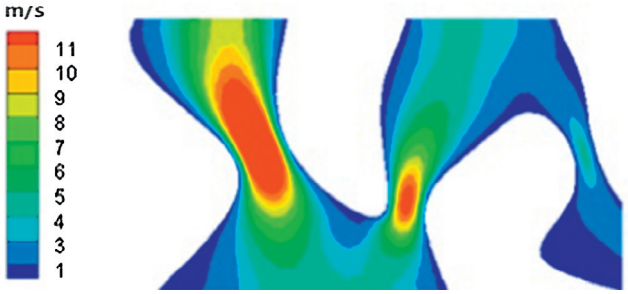


(b) 10kPa.

**Fig. 4.** Velocity contours of mixture after selection in the support layer of the composite membrane at different pressure differences.

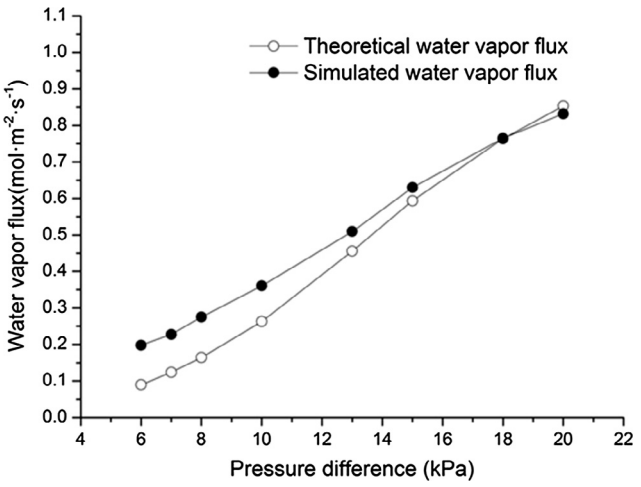


**Fig. 5.** Comparison of water vapor flux between the results by theoretical model and the numerical simulation.

**Table 2**
The water vapor penetration and selection for various membrane materials.

| Material | Permeability (Barrer) | Selectivity | | |
|---|---|---|---|---|
| | | ($H_2O/N_2$) | ($H_2O/O_2$) | ($H_2O/CO_2$) |
| Poly(ether sulphone) | 2620 | 10,500 | – | – |
| Polyimide | 640 | 5,330,000 | 888,000 | 200,000 |
| Poly(vinyl alcohol) | 19 | 3300 | 800 | 220 |
| Cellulose acetate | 6000 | 24,000 | 6000 | 1600 |
| Polysulphone | 2000 | 8000 | 1300 | 500 |

gas are 17.08%, 71.88%, 3.5% and 6.99%, respectively. The hollow fiber membrane is selected as the representative, which is composed of hollow pipes as shown in Fig. 1. The outside diameter of the hollow fiber membrane is 1.2 mm, and the inner diameter is 0.8 mm.

### 5.1. Effects of material and pressure

Polysulfone, cellulose acetate and polyimide were selected as the membrane material. The theoretical analysis are taken under the temperature of 383.15 K, the film porosity of 0.6, the thickness of connecting layer of 20 μm. The pressure difference is ranged 3–15 kPa. In the calculation, assume that the pressure gradient along the flue gas mass transfer direction distributes uniformly.

The influences of the membrane materials on the water recovery under different pressure difference are illustrated in Fig. 6. It can be obtained that the permeation of water vapor increases with the pressure difference. During the initial period of the pressure difference increasing, the variation of water vapor flux is not obvious due to the friction force between the gas and the membrane. It also can be found that the membrane material has a great influence on the flux of water vapor, especially the coating material, which has selectivity for different flue gas components. However, the water vapor flux under different material conditions does not simply proportional to the Henry coefficient. The reason is that the mass transfer mechanism of the supporting layer and the connecting layer is satisfied with the micro porous diffusion mechanism. Increasing the pressure difference, the water vapor flux is more obviously influenced by the solubility and permeability of the material.

Nevertheless, it is not all materials with larger amount of water vapor flux that is more suitable for engineering applications. Not only taking into account the cost of the material, but also considering whether the quality of water vapor can meet the requirements. As shown in Fig. 7, it can be seen that the purity of the water recycled by the membrane will be reduced with the pressure difference, and also is different for different membrane materials. If the water quality requirements are not high for industrial applications, the recovery water can be used directly. On the other hand, it will need a chemical treatment in further if the water is used for more demanding utilizations. At this situation, polyimide material can better meet the requirements although its water vapor flux is relatively lower than that of the other materials as shown in Fig. 6.

### 5.2. Effects of porosity

Effects of porosity are mainly reflected in the microscale diffusion effect, especially the Knudsen diffusion. In this section, the polyimide was selected as membrane material with the operating condition of temperature of 383.15 K, pressure difference of 6 kPa and connecting layer thickness of 200 μm. Fig. 8 shows the variation of water vapor flux through the composite membrane with the porosity of support layer changed from 0.4 to 0.8.

As shown in Fig. 8, the porosity has significant impact on the water vapor flux through the membrane. The flux of water vapor increases sharply with the porosity. However, the increment of the porosity leads to the reduction of the support performance of membrane, and hence reduces its mechanical properties, which affecting the service life of the membrane. Therefore suitable porosity should be selected by the comprehensive consideration of high water vapor flux and little loss of mechanical performance.

### 5.3. Effects of thickness of transition layer

The reason why the connecting layer can affect the water vapor permeation is that the increase of the penetration length of the membrane. Embedding rate is defined as,

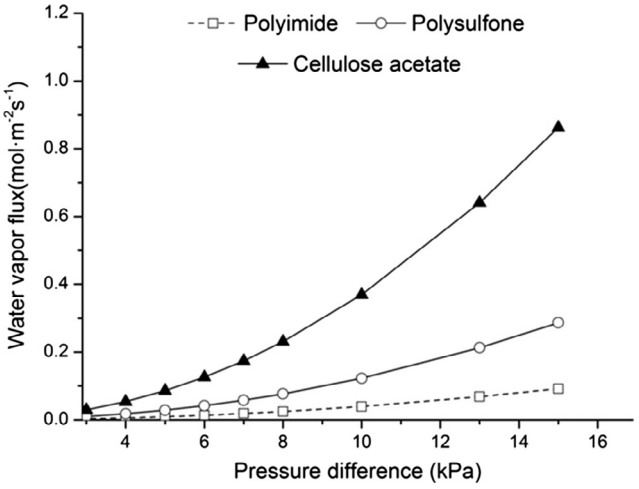


**Fig. 6.** Theoretical results of water vapor flux with pressure difference in three kinds of membrane materials.

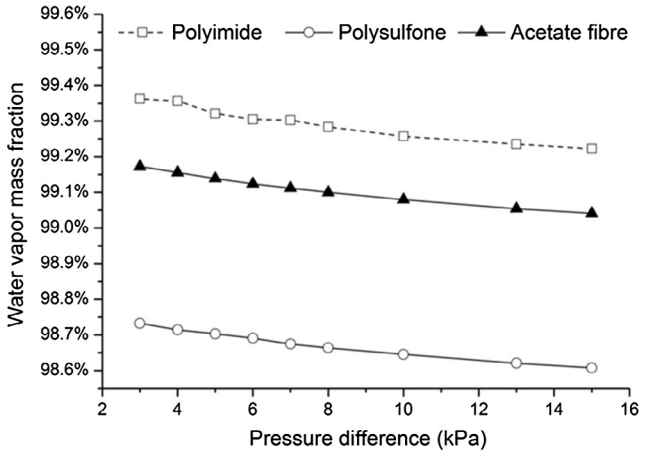


**Fig. 7.** Theoretical results of recycled water purity with pressure difference and membrane material.

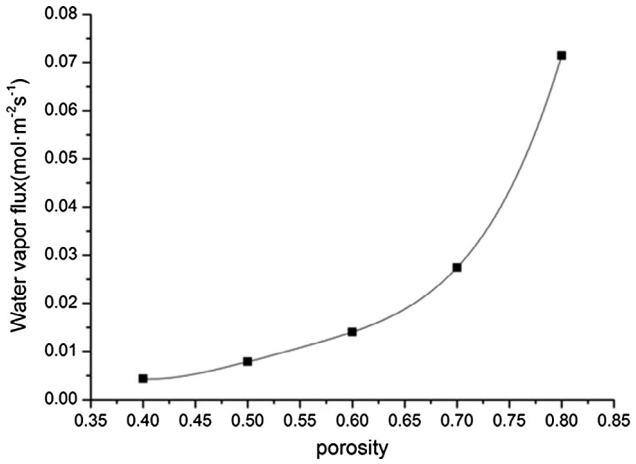


**Fig. 8.** Theoretical results of water vapor flux with the porosity of support layer.

$$f = \frac{L_2}{L} \tag{18}$$

in which, $L_2$ and $L$ are the connecting layer and whole membrane thickness, respectively. Under the premise that the total thickness, $L$, is constant, Fig. 9 shows the variation of the water vapor flux through the membrane with the embedding rate. Relatively, the thickness of transition layer has less affect on the water recovery than that of the porosity. However, it is found that the water vapor flux has little increase with increasing the embedding rate, i.e., the thickness of the transition layer. Because of the change of $f$, the proportion of the three structures has changed. Increasing the thickness of the transition layer makes the selection of the performance increase.

Also it is found that the water vapor flux has a faster increment while the embedding rate is below 0.15. While the embedding rate is larger than 0.2, the growth rate of water vapor flux is relatively slow. It is similar to the increase of porosity that the mechanical property of the membrane can be weakened with the high embedding rate. Despite of the little improvement in water recovery, it is not favorable for a long time practical application.

### 5.4. Membrane material selections for practical application

The present theoretical model also can be referenced in the selection of membrane materials, the selection of operating conditions and other aspects. As for choosing membrane materials, material selection performance, water vapor permeability, mechanical properties, economy, operating pressure and other conditions are important to make a decision, which belongs to the category of multiple attribute decision making problems [29,30].

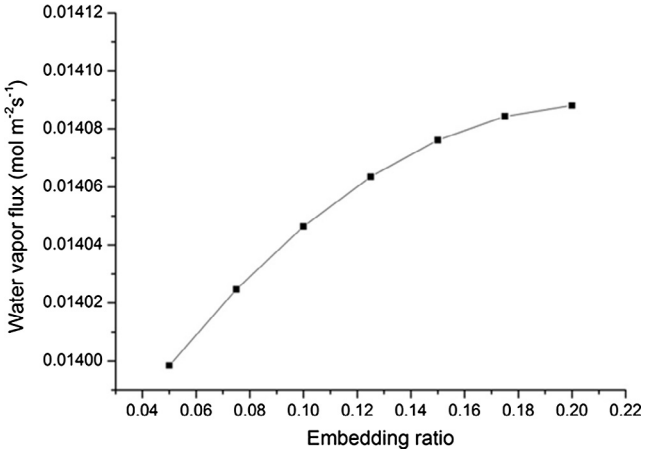


**Fig. 9.** Theoretical results of water vapor flux with embedding rate.

Collecting selectivity, permeability, price and impact stress data of six kinds of materials, such as polyimide and acetate fiber, the water vapor flux through the membrane and gas recovery steam percentage were calculated by using the previous model and calculation process. Under the conditions as follows, 0.6 of porosity, 10 kPa of pressure difference, 383.15 K of the exhaust flue inlet temperature and 20 μm of connecting layer thickness, the results of the six kinds of materials obtained are listed in Table 3.

According to the table an evaluation index matrix can be obtained, and with which one can preprocess the data. The water vapor flux and the percentage of water vapor belong to the benefit attribution, the price belongs to the cost attribution. Due to the impact strength and tensile strength show an inverse relationship in most cases, the impact strength neither belongs to benefit nor cost attribute.

The TOPSIS [31,32] was employed to make decision analysis. The algorithm steps are as follows.

Firstly, find a standardized decision-making matrix by the method of vector normalization. Its expression is,

$$g_{mn} = \frac{y_{mn}}{\sqrt{\sum_{m=1}^{s} y_{mn}^2}} \tag{19}$$

in which, $y_{mn}$ represents attribute value of row $m$ and column $n$. $g_{mn}$ is the value after vector specification, and $s$ is the number of data.

Construct weighted norm matrix $H = \{h_{mn}\}$ and set the weight of row $m$ and column $n$ as $w_{mn}$, then, the weighted standard value is written as,

$$h_{mn} = w_{mn} g_{mn} \tag{20}$$

Determine the positive and negative ideal solution. For the benefit type attribute, the positive and negative ideal solutions are shown as Eqs. (21) and (22), and cost attribute value represents contrary,

$$h_n^+ = \max h_{mn} \tag{21}$$

$$h_n^- = \min h_{mn} \tag{22}$$

in which, $h_n{}^+$, $h_n{}^-$ are maximum and minimum values of h, respectively.

Then, the distance between each solution to the positive and negative ideal solution is calculated, shown as $d_m{}^+$, $d_m{}^-$, respectively,

$$d_m^+ = \sqrt{\sum\nolimits_{n=1} (h_{mn} - h_n^+)^2} \tag{23}$$

$$d_m^- = \sqrt{\sum\nolimits_{n=1} (h_{mn} - h_n^-)^2} \tag{24}$$

The comprehensive evaluation index of each plan is shown as follow,

$$C_m^* = d_m^- / (d_m^- + d_m^+) \tag{25}$$

Finally, according to $C_m{}^*$ which means the comprehensive evaluation index, the material selection order can be obtained.

Based on Eq. (19), the value of the vector specification is listed in Table 4.

Using entropy weight method [33] to determine the weight of each attribution. The entropy of each evaluation index is defined as,

**Table 3**
Performance of the different membrane materials.

| | Water vapor flux (mol/m$^2$ s) | Percentage of water vapor (%) | Price (RMB¥/kg) | Impact strength (kJ/m$^2$) |
|---|---|---|---|---|
| 1 Polyimide | 0.01345 | 99.3049 | 95 | 28 |
| 2 Polysulfone | 0.04183 | 98.6908 | 48 | 206 |
| 3 Acetate fiber | 0.12592 | 99.1241 | 45 | 68 |
| 4 Polyethersulfone | 0.00961 | 99.5904 | 98 | 78 |
| 5 Ethyl cellulose | 0.02222 | 99.5962 | 62 | 21 |
| 6 PEEK | 0.22372 | 99.6021 | 350 | 70 |

**Table 4**
Vector specification attribution.

| | $g_1$ ($y_1$) | $g_2$ ($y_2$) | $g_3$ ($y_3$) | $g_4$ ($y_4$) |
|---|---|---|---|---|
| 1 Polyimide | 0.05142 | 0.40819 | 0.24586 | 0.44507 |
| 2 Polysulfone | 0.15991 | 0.40567 | 0.12422 | 0.00000 |
| 3 Acetate fiber | 0.48139 | 0.40745 | 0.11646 | 0.51354 |
| 4 Polyethersulfone | 0.03673 | 0.40937 | 0.25363 | 0.48194 |
| 5 Ethyl cellulose | 0.08496 | 0.40939 | 0.16046 | 0.20542 |
| 6 PEEK | 0.85527 | 0.40941 | 0.90581 | 0.51354 |

$$W_n = -\left(\sum_{m=1}^{s} f_{mn} \ln f_{mn}\right) / \ln k \tag{26}$$

in which, $W_n$ is the entropy value, and $f_{mn}$ is a dimensionless number which can be written as,

$$f_{mn} = (1 + z_{mn}) / \sum_{m=1}^{s} (1 + z_{mn}) \tag{27}$$

The entropy weight of the index $m$ is obtained by,

$$w_n = (1 - W_n) / \left(s - \sum_{n=1}^{s} W_n\right) \tag{28}$$

Due to the requirements of the various indicators are not the same, combining the objective entropy weight method and the subjective expert scoring method. The comprehensive weight is,

$$t_{mn} = \frac{\lambda_m w_m}{\sum_{m=1}^{s} \lambda_m w_m} \tag{29}$$

in which, *tmn* is the comprehensive weight, and $\lambda$ represents expert weight.

From the datas listed in Table 4 we can obtain the entropy weight, $w = \{4.5275 \times 10^{-1}, \ 8.3313 \times 10^{-6}, \ 3.6027 \times 10^{-1}, \ 1.8698 \times 10^{-1}\}$. The subjective weight is determined by the important degree of each attribution, $\lambda = \{0.3, 0.3, 0.3, 0.1\}$. The comprehensive weight vector can be then acquired as, $\tau = \{5.1722 \times 10^{-1}, \ 9.5177 \times 10^{-6}, \ 4.1157 \times 10^{-1}, \ 7.1201 \times 10^{-2}\}$

The weighted standard value can be calculated by Eq. (20), of which the results is shown in Table 5.

The distance between each solution to the positive and negative ideal solution is calculated, and the results are shown in Table 6. By the value of the queue size $C_i^*$, the acetate fiber is the optimal selection as the water recovery material under the present conditions. It's water flux is high and is much cheaper than PEEK, it has a higher advantage in industrial applications. So acetate fiber is suitable to recycle water vapor. If the requirements of water vapor with high flux material and the price is not so important, or requiring water quality to meet stringent standards, then there will be a different choice.

**Table 6**
Positive, negative distance and queuing indication.

| | $d_i^*$ | $d_i^0$ | $C_i^*$ |
|---|---|---|---|
| 1 Polyimide | 0.0546 | 0.0350 | 0.3906 |
| 2 Polysulfone | 0.0471 | 0.0420 | 0.4715 |
| 3 Acetate fiber | 0.0252 | 0.0515 | 0.6713 |
| 4 Polyethersulfone | 0.0557 | 0.0346 | 0.3836 |
| 5 Ethyl cellulose | 0.0521 | 0.0395 | 0.4312 |
| 6 PEEK | 0.0416 | 0.0554 | 0.5710 |

## 6. Conclusions

The Maxwell Stefan theory was employed to model the water vapor separation from the flue gas of lignite boiler by typical composite membrane. The composite membrane was divided into three parts including that of coating layer, connecting layer and supporting layer. The influences of coating material, pressure difference, porosity and embedding rate value on the water vapor mass transfer were analyzed. The following conclusions can be obtained.

(1) Materials has large effects on water vapor mass transfer. The material selection needs to be guaranteed higher water vapor selectivity under the premise of larger permeability.

**Table 5**
Weighted standard value matrix.

| | $h_1$ | $h_2$ | $h_3$ | $h_2$ |
|---|---|---|---|---|
| 1 Polyimide | $7.0904 \times 10^{-2}$ | $1.5862 \times 10^{-6}$ | $6.5684 \times 10^{-2}$ | $1.2610 \times 10^{-2}$ |
| 2 Polysulfone | $7.8221 \times 10^{-2}$ | $1.5834 \times 10^{-6}$ | $5.9271 \times 10^{-2}$ | $8.7261 \times 10^{-3}$ |
| 3 Acetate fiber | $9.9900 \times 10^{-2}$ | $1.5854 \times 10^{-6}$ | $5.8862 \times 10^{-2}$ | $1.3207 \times 10^{-2}$ |
| 4 Polyethersulfone | $6.9914 \times 10^{-2}$ | $1.5875 \times 10^{-6}$ | $6.6093 \times 10^{-2}$ | $1.2932 \times 10^{-2}$ |
| 5 Ethyl cellulose | $7.3167 \times 10^{-2}$ | $1.5876 \times 10^{-6}$ | $6.1181 \times 10^{-2}$ | $1.0519 \times 10^{-2}$ |
| 6 PEEK | $1.2511 \times 10^{-1}$ | $1.5876 \times 10^{-6}$ | $1.0048 \times 10^{-1}$ | $1.3207 \times 10^{-2}$ |

(2) In the range of mechanical properties, pressure difference, porosity and the embedding rate contribute to improve the water vapor flux.
(3) Using multiple attribute decision making method, the case study reveals that the acetate fiber is the optimal selection as the water recovery material for potential engineering applications, which can achieve both high water flux and cheap cost.

## Conflict of interest

The authors declared that there is no conflict of interest.

## Acknowledgments

The financial supports for this research project from the National Natural Science Foundation of China (No. 51676069) and the National "973 Program" of China (No. 2015CB251503) are gratefully acknowledged.

## References

[1] Katerina Setnickova, Vladimir Sima, Roman Petrychkovych, Separation of gas mixtures by new type of membranes – dynamic liquid membranes, Sep. Purif. Technol. 160 (2016) 132–135.
[2] Yan Dai, Xuehua Ruan, Feng Bai, Yu. Miao, Hao Li, Zongchang Zhao, Gaohong He, High solvent resistance PTFPMS/PEI hollow fiber composite membrane for gas separation, Appl. Surf. Sci. 360 (2016) 164–173.
[3] Nikolay Kosinov, Jorge Gascon, Freek Kapteijn, Emiel.J.M. Hensen, Recent developments in zeolite membranes for gas separation, J. Membr. Sci. 499 (2016) 65–79.
[4] H. Mohammad, Murad Chowdhury, Xianshe Feng, Peter Douglas, Eric Croiset, A new numerical approach for a detailed multicomponent gas separation membrane model and AspenPlus simulation, Chem. Eng. Technol. 28 (7) (2005) 773–782.
[5] Brian Bolto, Manh Hoang, Zongli Xie, A review of water recovery by vapor permeation through membranes, Water Res. 46 (2012) 259–266.
[6] Haiqing Lin, Scott M. Thompson, Adrian Serbanescu Martin, Johannes G. Wijmans, Karl D. Amo, Kaaeid A. Lokhandwala, Timothy C. Merkel, Dehydration of natural gas using membranes. Part I: Composite membranes, J. Membr. Sci. 413–414 (2012) 70–81.
[7] Recep Kaya, Gokhan Deveci, Turker Turken, Reyhan Sengur, Serkan Guclu, Derya Y. Koseoglu-lmer, Analysis of wall shear stress on the outside-in type hollow fiber membrane modules by CFD simulation, Desalination 351 (2014) 109–119.
[8] Hylke Sijbesma, Kitty Nymeijer, Rob van Marwijk, Matthias Wessling, Flue gas dehydration using polymer membranes, J. Membr. Sci. 313 (2008) 263–276.
[9] Cheng-Xian Lin, Dexin Wang, Ainan Bao, Numerical modeling and simulation of condensation heat transfer of a flue gas in a bundle of transport membrane tubes, Int. J. Heat Mass Transfer. 60 (2013) 41–45.
[10] Chunhong He, Study on separation of organic vapor/nitrogen system through composite hollow fiber membrane, Tianjin: Tianjin University, Ph.D Thesis, 2006 (in Chinese).
[11] R.W. Schofield, A.G. Fane, C.J.D. Fell, Gas and vapour transport through microporous membranes. I: Knudsen-poiseuille transition, J. Membr. Sci. 53 (1990) 159–171.
[12] Rong Wang, Tai-Shung Chung, Determination of pore sizes and surface porosity and the effect of shear stress within a spinneret on asymmetric hollow fiber membranes, J. Membr. Sci. 188 (2001) 29–37.
[13] A. Bertei, C. Nicolella, Common inconsistencies in modeling gas transport in porous electrodes: the dusty-gas model and the Fick law, J. Power Sources 279 (2015) 133–137.
[14] J.A. Wesselingh, R. Krishna, Mass Transfer in Multicomponent Mixture, Delft University Press, 2000.
[15] M. Grahn, J. Hedlund, Maxwell-Stefan modeling of high flux tubular silicalite-1 membranes for $CO_2$ removal from $CO_2/H_2$ gas mixtures, J. Membr. Sci. 471 (2014) 328–337.
[16] Jani Kangas, Linda Sandstrom, Ilkka Malinen, Jonas Hedlund, Ju.ha. Tanskanen, Maxwell-Stefan modeling of the separathion of $H_2$ and $CO_2$ at high pressure in an MFI membrane, J. Membr. Sci. 435 (2013) 186–206.
[17] A. Costa-Corredor, Z. Pakowski, T. Lenczewski, P. Gou, Simulation of simultaneous water and salt diffusion in dry fermented sausages by the Stefan-Maxwell equation, J. Food Eng. 97 (2010) 311–318.
[18] Rajamani Krishna, Jasper M. van Baten, Maxwell-Stefan modeling of slowing-down effects in mixed gas permeation across porous membranes, J. Membr. Sci. 383 (2011) 289–300.
[19] Yan Sun, Kun Yang, Analysis of mass transport models based on Maxwell-Stefan theory and Fick's law for protein uptake to porous anion exchanger, Sep. Purif. Technol. 60 (2008) 180–189.
[20] R. Suwanwarangkul, E. Croiset, M.W. Fowler, P.L. Douglas, E. Entchev, M.A. Douglas, Performance comparison of Fick's, dusty-gas and Stefan-Maxwell models to predict the concentration over potential of a SOFC anode, J. Power Sources 122 (2003) 9–18.
[21] Dexin Wang, Ainan Bao, Walter Kuncet, William Liss, Coal power plant flue gas waste heat and water recovery, Appl. Energy 91 (2012) 34l–348.
[22] Lloyd S. White, Xiaotong Wei, Saurabh Pande, Wu. Tony, Timothy C. Merkel, Extended flue gas trials with a membrane-based pilot plant at a one-ton-per-day carbon capture rate, J. Membr. Sci. 496 (2015) 48–57.
[23] Gh. Bakeria, A.F. Ismailb, M. Rahimnejada, T. Matsuura, Porous polyethersulfone hollow fiber membrane in gas–liquid contacting processes, Chem. Eng. Res. Des. 92 (2014) 1381–1390.
[24] J.W. Veldsink, R.M.J. van Damme, G.F. Versteeg, W.P.M. van Swaaij, The use of dusty-gas model for the description of mass transport with chemical reaction in porous media, Chem. Eng. J. 57 (2) (1995) 115–125.
[25] P.J.A.M. Kerkhof, A modified Maxwell-Stefan model for transport through inert membranes: the binary friction model, Chem. Eng. J. 64 (1996) 319–343.
[26] N. Dongari, Y. Zhang, J.M. Reese, Modeling of Knudsen layer effects in micro/nanoscale gas flows, ASME J. Fluid Eng. 133 (2011) 071101.
[27] Sybrand J. Metz, W.J.C. van de Ven, J. Potreck, M.H.V. Mulder, Matthias Wessling, Transport of water vapor and inert gas mixtures through highly selective and highly permeable polymer membranes, J. Membr. Sci. 251 (1–2) (2005) 29–41.
[28] S.J. Metz, W.J.C. van de Ven, J. Potreck, M.H.V. Mulder, Matthias Wessling, Transport of water vapor and inert gas mixtures through highly selective and highly permeable polymer membranes, J. Membr. Sci. 251 (2005) 29–41.
[29] Pengbo Sun, Yutian Liu, Xizhao Qiu, Hybrid multiple attribute group decision-making for power system restoration, Expert Syst. Appl. 42 (2015) 6796–6805.
[30] Jindong Qin, Xinwang Liu, Multi-attribute group decision making using combined ranking value under interval type-2 fuzzy environment, Info. Sci. 297 (2015) 293–315.
[31] Xiaoxia Wang, Fengbao Yang, Hong Weib, Lei Zhang, A new ranking method based on TOPSIS and possibility theory for multi-attribute decision making problem, Optik 126 (2015) 4852–4860.
[32] Deepa Joshi, Sanjay Kumar, Interval-valued intuitionistic hesitant fuzzy Choquet integral based TOPSIS method for multi-criteria group decision making, Eur. J. Oper. Res. 248 (2016) 383–391.
[33] Xiaowen Qi, Changyong Liang, Junling Zhang, Generalized cross-entropy based group decision making with unknown expert and attribute weights under interval-valued intuitionistic fuzzy environment, Comput. Ind. Eng. 79 (2015) 52–64.